Chinese Chemical Letters 34 (2023) 108512

Contents lists available at ScienceDirect

Chinese Chemical Letters

journal homepage: www.elsevier.com/locate/cclet

Resistive-type sensors based on few-layer MXene and SnO_2 hollow spheres heterojunctions: Facile synthesis, ethanol sensing performances

Lihua Chu[a], Hao Yan[a], Wanfeng Xie[b,c,*], Yuxin Shi[a], Muhammad Hilal[c], Changxu Sun[a], Ze Li[a], Meicheng Li[a,*]

[a] School of New Energy, North China Electric Power University, Beijing 102206, China
[b] College of Electronics and Information, University-Industry Joint Center for Ocean Observation and Broadband Communication, Qingdao University, Qingdao 266071, China
[c] Department of Physics, Dongguk University, Seoul 04620, Republic of Korea

ARTICLE INFO

Article history:
Received 8 March 2023
Revised 20 April 2023
Accepted 26 April 2023
Available online 28 April 2023

Keywords:
Heterostructure
Few-layer MXene
SnO_2 hollow spheres
Ethanol sensor
Synergistic effect
$SnO_2/Ti_3C_2T_x$ composites

ABSTRACT

High-performance and low-cost gas sensors are highly desirable and involved in industrial production and environmental detection. The combination of highly conductive MXene and metal oxide materials is a promising strategy to further improve the sensing performances. In this study, the hollow SnO_2 nanospheres and few-layer MXene are assembled rationally *via* facile electrostatic synthesis processes, then the $SnO_2/Ti_3C_2T_x$ nanocomposites were obtained. Compared with that based on either pure SnO_2 nanoparticles or hollow nanospheres of SnO_2, the $SnO_2/Ti_3C_2T_x$ composite-based sensor exhibits much better sensing performances such as higher response (36.979), faster response time (5 s), and much improved selectivity as well as stability (15 days) to 100 ppm C_2H_5OH at low working temperature (200 °C). The improved sensing performances are mainly attributed to the large specific surface area and significantly increased oxygen vacancy concentration, which provides a large number of active sites for gas adsorption and surface catalytic reaction. In addition, the heterostructure interfaces between SnO_2 hollow spheres and MXene layers are beneficial to gas sensing behaviors due to the synergistic effect.

Volatile organic compounds (VOCs), CO_x and NO_x (x = 1, 2), *etc.*, mainly come from industrial waste gas, automobile exhaust, and photochemical pollution. And these exhaust gases have a serious and adverse effect on the living environment and the human body [1]. As far as ethanol is concerned, long-term exposure to this volatile toxic substance will not only irritate the eyes and damage the skin and respiratory system but also weaken the function of the central nervous system and even threaten people's life and health [2]. Therefore, exploring novel and effective gas sensing materials to prepare ethanol sensors with fast response, rapid recovery, and long-term stability is particularly important for industrial production and human health.

In recent years, metal-oxide-semiconductors (MOS)-based gas sensors have been widely used to detect toxic gases due to their easy fabrication, excellent properties, and low cost. For example, SnO_2 (E_g = 3.6 eV) and ZnO (E_g = 3.7 eV), as n-type semiconductors, have high carrier concentration, mobility, and excellent chemical stability, which have been proved to be excellent gas sensing materials [3,4]. As a traditional sensing semiconductor material, the conductivity of SnO_2 can be adjusted *via* controllable morphology modification, surface decoration, and doping methods, which are widely adopted in the detection of ethanol or other VOCs [5,6]. However, the low response, high operating temperature, and limited selectivity still restrict the widespread application of SnO_2 in gas sensors [3]. To further improve the gas sensing performances of SnO_2 to ethanol detection, many researchers control the reaction conditions to modulate the microscopic morphology of the material, which can effectively increase its specific surface area [7,8]. Also, some researchers have improved its gas-sensing response by doping with metal elements, especially noble metals and constructing heterojunctions [9–11]. Synthesizing composites of SnO_2 with suitable electrical conductivity is a promising strategy to obtain SnO_2 and its composites with better sensing properties like a high response, good selectivity, and fast response/recovery times [12].

* Corresponding authors.
E-mail addresses: wfxie@qdu.edu.cn (W. Xie), mcli@ncepu.edu.cn (M. Li).

https://doi.org/10.1016/j.cclet.2023.108512
1001-8417/

MXene, an emerging family of 2D transition metal carbides/nitride materials, is widely used in the field of sensing, catalysis, and energy storage because of its large specific surface area and excellent electronic conductivity [13,14]. MXene is terminated by functional groups of –F, –O and –OH. These functional groups at the terminals provide a large number of active sites for target gas adsorption. Few-layer MXene exhibits superior conductivity and gas sensing capabilities compared to multilayer bulk materials due to its larger specific surface area and increased active gas adsorption sites. This is attributed to the expanded interlayer spacing in few-layer MXene, which promotes electron transport and surface reactions, resulting in improved electrical and gas-sensitive properties. At present, studies have shown that accordion-shaped or clay-shaped multi-layer MXene and few-layer or single-layer MXene have been successfully applied in gas detection [14,15]. The composites composed of MXene ($Ti_3C_2T_x$) nanosheets and transition metal sulphide (WSe_2) nanoflakes are prepared by electrostatic self-assembly in the liquid phase [16]. The hybridization process provides an effective strategy against MXene oxidation and the formation of continuous heterostructures on the material surface, which significantly improves its gas sensing performance and reduce the response/recovery times. However, there are few reports on the electrostatic self-assembly of MXene and topography-controlled SnO_2 to improve the gas-sensing properties of ethanol.

This work presents an ethanol gas sensor based on the $SnO_2/Ti_3C_2T_x$ composites, which are rarely synthesized *via* the electrostatic self-assembly strategy. Here, the SnO_2 hollow spheres are uniformly distributed on the surface of few-layer MXene nanosheets. Moreover, the response performances of composites to ethanol are systematically investigated. The results show that $SnO_2/Ti_3C_2T_x$ composites have significantly improved gas-sensitive properties to ethanol compared with pure SnO_2 counterpart. At 200 °C, the response value of $SnO_2/Ti_3C_2T_x$ composites to 100 ppm ethanol gas can reach 36.979, which is 4.16 times higher than that of pure SnO_2 under the same conditions, and the response/recovery times are reduced obviously. According to the classical depletion layer model [17,18], the remarkable gas sensing properties of the composites rely on its unique layer architecture. MXene provides a unique platform on which hollow nanospheres of SnO_2 can be decorated to form heterojunctions, significantly enlarging the specific surface area and increasing oxygen vacancy concentration, thus considerably enhancing the gas sensing performances.

The composites were prepared by the electrostatic self-assembly method [19]. Typically, 120 mg of hollow SnO_2 nanospheres were added into 20 mL 1% cetyltrimethylammonium bromide (CTAB) aqueous solution and dispersed by ultrasonication for 8 h. After that, the precipitates were collected by centrifugation. Then, 20 mg of the prepared few-layer $Ti_3C_2T_x$ MXene were dissolved in 20 mL deionized water and dispersed ultrasonically for 30 min under argon protection, the two products are then mixed together and left to stand for 24 h under the protection of argon. The precipitates were collected by centrifugation and dried at 70 °C for 12 h to obtain $SnO_2/Ti_3C_2T_x$ composites. The complete preparation process is shown in Fig. 1.

The crystal structure of the prepared MXene, pure SnO_2 nanoparticles or hollow nanospheres, and $SnO_2/Ti_3C_2T_x$ composites were analyzed by X-ray powder diffraction (XRD). The diffraction peaks of Ti_3AlC_2 MAX phase and $Ti_3C_2T_x$ MXene are shown in Fig. 2a. The characteristic peaks of the unetched Ti_3AlC_2 materials match well with the standard card (JCPDS No. 52-0875). After etching, the (002) peak of Ti_3AlC_2 at 9.5° shifted to 6.58° for the $Ti_3C_2T_x$ in XRD patterns, and the layer spacing became 13.4 Å. The lower peak shift of the basal plane is due to the removal of Al in the Ti_3AlC_2 and the introduction of surface terminal groups in $Ti_3C_2T_x$ (*e.g.*, -F, –O, –OH). The crystal structure of pure

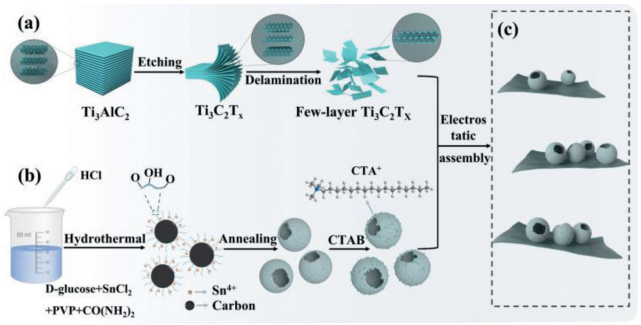

Fig. 1. Schematic formation of $SnO_2/Ti_3C_2T_x$ composites.

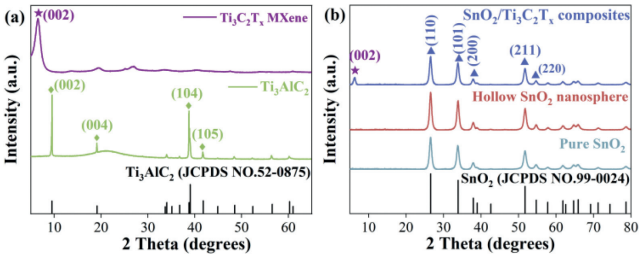

Fig. 2. XRD patterns of (a) Ti_3AlC_2 MAX phase and $Ti_3C_2T_x$ MXene, (b) pure SnO_2, hollow SnO_2 nanosphere, and $SnO_2/Ti_3C_2T_x$ composites.

SnO_2, hollow SnO_2 nanosphere, and $SnO_2/Ti_3C_2T_x$ composites are shown in Fig. 2b. The diffraction peaks of SnO_2 samples at 26.58°, 33.85°, 37.89° and 51.84° correspond to (110), (101), (200) and (211), respectively, which well matched with PDF card (JCPDS No. 99-0024), indicating that the hollow SnO_2 nanospheres with tetragonal rutile structure have been successfully prepared [20]. Compared with the pure SnO_2, $SnO_2/Ti_3C_2T_x$ composites have a pronounced diffraction peak at $2\theta = 6.20°$, which corresponds to the (002) crystal plane of MXene, indicating that $SnO_2/Ti_3C_2T_x$ composites have been successfully obtained.

As shown in Fig. 3a, the etched MXene exhibits a few-layer structure. The prepared MXene micron-scale sheets with sizes

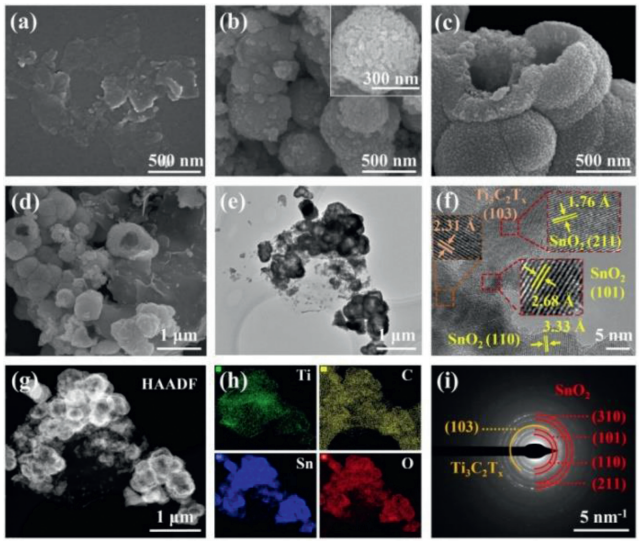

Fig. 3. Microstructures of the obtained samples: SEM images of (a) few-layer MXene, (b) SnO_2 nanospheres, (c) hollow SnO_2 nanospheres, (d) $SnO_2/Ti_3C_2T_x$ composites. (d) TEM and (f) HRTEM images of the composites. (g) HAADF and (h) element distribution images of the composites; (i) corresponding SAED patterns of the composites.

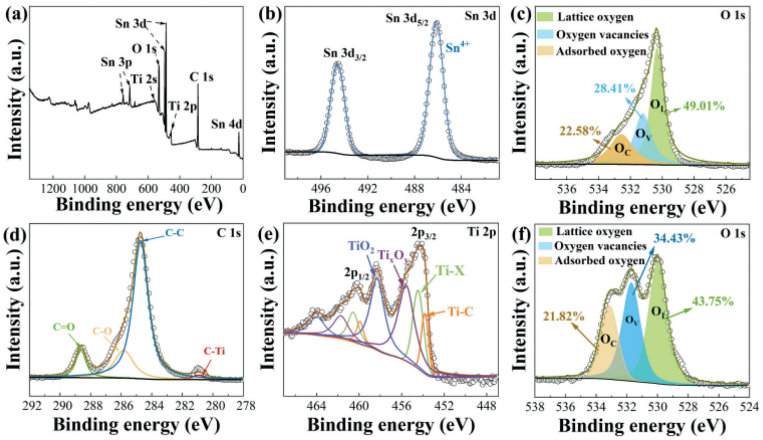

Fig. 4. (a) XPS fully scanned spectra of $SnO_2/Ti_3C_2T_x$ composites, XPS spectra of (b) Sn 3d (c) O 1s in pure SnO_2, XPS spectra of (d) C 1s, (e) Ti 2p and (f) O 1s in $SnO_2/Ti_3C_2T_x$ composites.

of approximately 600–700 nm have several features for uniform distribution, easy stacking and flexible folding [21]. In Fig. 3b, the SnO_2 nanospheres with a size of about 500 nm were composed of agglomerates of small nanospheres (42 nm) in hydrothermal synthesis. After adding the glucose during the hydrothermal synthesis, the size of the formed hollow nanospheres increased significantly (from 500 nm to 600–700 nm), and the wall thickness is about 226 nm (Fig. 3c). The reason for this phenomenon may be that the carbon sphere template was formed during the hydrothermal process. It can be seen from Figs. 3d and e that SnO_2 nanospheres are uniformly distributed on the surface of $Ti_3C_2T_x$ few-layer nanosheets with slight agglomeration. The MXene nanosheets exhibit a few-layer structure and the SnO_2 nanospheres have a hollow structure from the TEM analysis (Fig. 3e).

More detailed morphological and structural analyses of the $SnO_2/Ti_3C_2T_x$ composites are shown in the HR-TEM images, as seen in Fig. 3f. The lattice fringe distances of 3.33, 2.68 and 1.76 Å correspond to the (110), (101) and (211) planes of rutile SnO_2, respectively [22]. A lattice spacing of 2.31 Å matches well with the (103) plane of $Ti_3C_2T_x$ MXene [23]. As shown in Figs. 3g and h, the high angle annular dark field (HAADF), and element distribution images show that the elements C, Ti, Sn and O are uniformly distributed in the composites. Moreover, the selected area electron diffraction (SAED) image is predicted in Fig. 3i, which shows that there is a clear polycrystalline diffraction ring. The diffraction ring marked in red corresponds to the (110), (101), (211) and (310) crystal plane of rutile SnO_2 from inside to outside, and the diffraction ring marked in yellow corresponds to the (103) crystal plane of $Ti_3C_2T_x$ MXene, which are consistent with the crystal data of XRD and HRTEM results.

The chemical composition of as-prepared samples was analyzed by X-ray photoelectron spectroscopy (XPS) (Fig. 4). In Fig. 4a, the XPS survey spectrum of the composites shows the characteristic peak of Sn 3d, O 1s, Ti 2p, and C 1s, which further confirms that the elements in the $SnO_2/Ti_3C_2T_x$ composites are composed of Sn, O, Ti and C. In Fig. 4b, the Sn 3d energy level spectra consists of two peaks at 486.56 eV and 494.96 eV, which belong to Sn $3d_{5/2}$ and Sn $3d_{3/2}$, respectively, indicating that Sn exists in the form of +4 in SnO_2 [24]. Fig. 4c shows the characteristic peaks of O 1s. The peaks at 530.1, 531 and 533.2 eV can be assigned to the lattice oxygen (O_L), oxygen vacancy (O_V) and chemisorbed oxygen (O_C), respectively [25]. Furthermore, the proportions of O_L, O_V, and O_C in pure SnO_2 are 49.01%, 28.41% and 22.58%, while the proportions of O_L, O_V and O_C in the $SnO_2/Ti_3C_2T_x$ composites are 43.75%, 34.43% and 21.82%, respectively (Fig. 4f). When SnO_2 is compounded with $Ti_3C_2T_x$ MXene, the concentration of O_V increases from 28.41% to 31.43%. The unique three-dimensional layered hollow-sphere composites architecture the lattice mismatch at the interface, and the homogeneous heterojunctions formed on the surfaces of the MXene and SnO_2 composite materials may all contribute the concentration of oxygen vacancies, and the study shows that the concentration of oxygen vacancies is critical to gas sensing performance [26]. In high-resolution XPS spectra of C 1s (Fig. 4d), the peaks at 280.96, 284.76, 285.81, 288.67 eV are attributed to C–Ti, C–C, C–O and O=C–O, respectively [27]. The C–C bond is the source of the main signal center of C 1s, and the diffraction peak at 284.81 eV represents the C–Ti bond, which proves the existence of MXene in the composites [28]. As shown in Fig. 4e, the Ti 2p core level is fitted with four doublets (Ti $2p_{3/2}$ – Ti $2p_{1/2}$). The binding energy of 458.32 eV corresponds to the Ti^{4+} in the composites, which means that TiO_2 is formed by oxidation during the synthesis process. The Ti $2p_{3/2}$ components are located at 455.60 eV as Ti ions with a reduced charge state (Ti_xO_y), and the 454.49 eV and 453.79 eV correspond to Ti-C bonds, substoichiometric titanium oxides, or carbides (Ti-X) [29]. Overall, XPS analysis shows that the composites were successfully prepared and the oxygen vacancy concentration increased with slight oxidation occurring in the synthesis process.

N_2 adsorption/desorption investigation was conducted to study the porous nature of pure SnO_2 and $SnO_2/Ti_3C_2T_x$ composites. As shown in Fig. 5, the adsorption/desorption isotherms of pure SnO_2 and $SnO_2/Ti_3C_2T_x$ composites exhibited typical IV and H3-type isotherms according to the IUPAC. In detail, the specific surface areas of pure SnO_2 and $SnO_2/Ti_3C_2T_x$ composites are 25.292 and 30.885 m^2/g, and their pore volumes are 0.106 and 0.129 cm^3/g, respectively. Further, the pore size distribution of pure SnO_2 and $SnO_2/Ti_3C_2T_x$ composites is 17.388 nm and 16.740 nm, respectively, demonstrating the mesoporous nature of $SnO_2/Ti_3C_2T_x$ composites. The large surface area of $SnO_2/Ti_3C_2T_x$ composites with unique micro-structures can provide more channels for the faster gases diffusion and more active sites for target gases adsorption, which

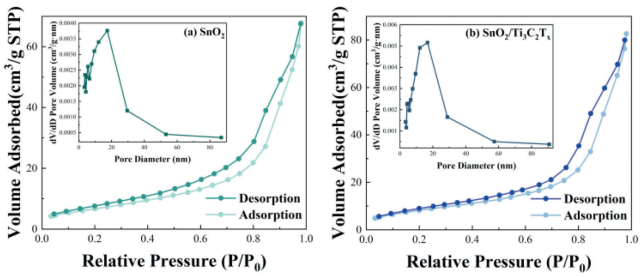

Fig. 5. N_2 isothermal adsorption/desorption curve, and the inset is the pore radius of pure SnO_2 and $SnO_2/Ti_3C_2T_x$ nanocomposites.

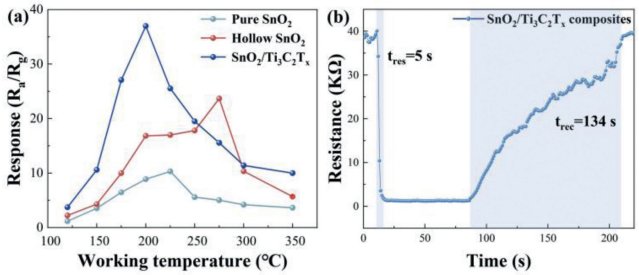

Fig. 6. (a) The responses of various samples to 100 ppm ethanol at different temperatures. (b) The response and recovery time of the $SnO_2/Ti_3C_2T_x$ composites sensors to 100 ppm ethanol at 200 °C.

achieve high gas sensing performance easily. The BET results indicate that the accessibility space of $SnO_2/Ti_3C_2T_x$ composites is larger, which means that the sensor based on the composites shows the highest response to ethanol [30].

The performances of sensing material are sensitive to their operating temperatures. First, the response value (R_a/R_g) versus operating temperature for pure SnO_2, hollow SnO_2 nanospheres, and the $SnO_2/Ti_3C_2T_x$ composites were carefully investigated toward 100 ppm ethanol. As shown in Fig. 6a, in the range from 120 °C to 350 °C, all curves show the same trend that the R_a/R_g increases first and then decreases sharply with the increase in temperature. In detail, at low operating temperature (from 120 °C to 200 °C), the activation energy is insufficient to overcome the potential barrier, so the response increases with increasing temperature. At higher temperatures such as above 200 °C, the desorption rate of gas molecules is higher than the adsorption rate, thus reducing the response [31,32]. The optimum working temperature of the $SnO_2/Ti_3C_2T_x$ composites is 200 °C, which is lower than that of pure SnO_2 (225 °C) and hollow SnO_2 (275 °C). The maximum R_a/R_g to 100 ppm ethanol gas is 10.306, 23.664 and 36.979 for pure SnO_2, hollow SnO_2 and $SnO_2/Ti_3C_2T_x$ composites, respectively. The dynamic response-recovery curve of the $SnO_2/Ti_3C_2T_x$ composites at the optimum operating temperature is shown in Fig. 6b. The resistance can be restored to the baseline from the atmosphere of ethanol gas to the fresh air. The response time is 5 s and the recovery time is 134 s, indicating that $SnO_2/Ti_3C_2T_x$ composites based sensor have a quick response characteristic.

To further investigate the sensing performances of $SnO_2/Ti_3C_2T_x$ composites, the prepared materials were exposed to the ethanol with the concentrations ranging from 10 ppm to 180 ppm at the optimal operating temperature of 200 °C, and the response behavior as a function of ethanol concentration is shown in Fig. 7a. The gas response value increases as the target gas concentration increases, and the composites have the best response performance to ethanol. In Fig. 7b, the linear fitting results show that the gas concentration and relative response satisfy the functional relationship of $R_{es} = 0.288C_{gas} + 6.456$, and the correlation coefficient (R^2) is 0.949, which indicates that the $SnO_2/Ti_3C_2T_x$ composites can be used in real-time monitoring of ethanol gas in industrial production, and can be used to quantitatively analyze the concentration range of ethanol gas, and detect lower concentrations of ethanol gas [33]. The repeatability of gas sensing materials is also essential for the sensors application. In Fig. 7c, the repeatability of the prepared materials is evaluated at the optimum working temperature. All the materials show excellent repetition, and the response dynamic curves of continuous tests are similar. Nevertheless, the composites exhibit faster and higher response and recovery characteristics towards 100 ppm ethanol gas. The dynamic curves of the response of $SnO_2/Ti_3C_2T_x$ composites show excellent recovery performance under different concentrations of the target gas, and the response value increases with increasing ethanol concentration

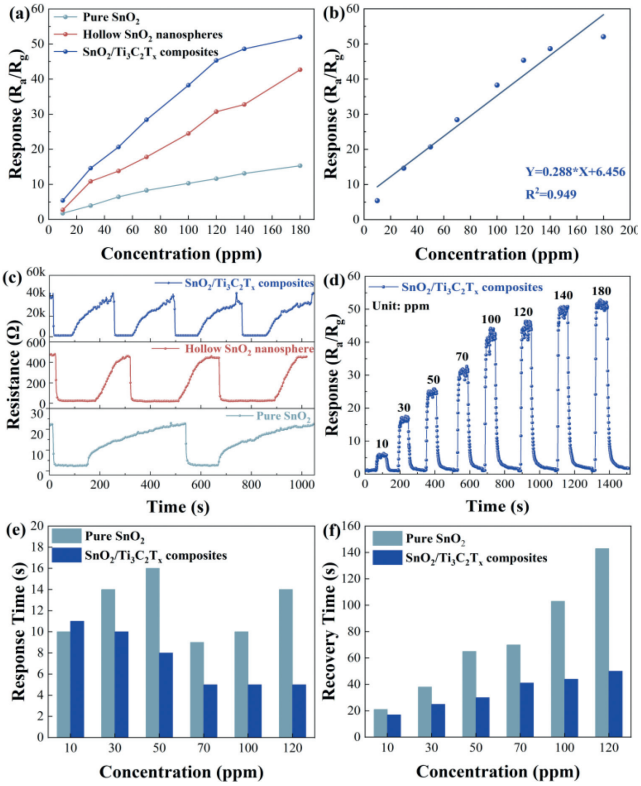

Fig. 7. (a) The responses of various samples upon exposure to ethanol with concentrations ranging from 10 ppm to 180 ppm. (b) Function fitting plots of the $SnO_2/Ti_3C_2T_x$ composites sensor towards different concentrations (10–180 ppm) of ethanol. (c) Repeatability curve of the various samples towards 100 ppm ethanol gas. (d) Dynamic response curves of the composite sensors towards ethanol gas with various concentrations ranging from 10 ppm to 180 ppm at 200 °C. (e) The response time and (f) recovery time of the pure SnO_2 and the $SnO_2/Ti_3C_2T_x$ composites across ethanol concentrations.

(Fig. 7d). When the concentration of ethanol reaches 140 ppm, the response value of the composites increases little with the further increase of ethanol concentration, which may be due to the limited number of active sites in the composites [34]. Figs. 7e and f are the response/recovery curves of the composites and pure SnO_2 to different concentrations of ethanol. The results show that the introduction of few-layer MXene nanosheets into the composites significantly shortens the response/recovery times, possibly because the metallic conductivity of MXene nanosheets significantly shortens the carrier transport time. Therefore, the response and recovery properties of composites are significantly improved [13].

In addition, selectivity and long-term stability are also important factors for the gas sensors. The sensing responses of pure SnO_2 and $SnO_2/Ti_3C_2T_x$ composites to 100 ppm ethanol, methanol, acetone, ammonia, and chlorobenzene are tested at 200 °C as shown in Fig. 8a. The response of the composites is 36.979 (ethanol), 6.069 (methanol), 4.809 (acetone), 1.616 (ammonia) and 2.125 (chlorobenzene), respectively, which indicates good selectivity of composites to ethanol among the tested gas molecules. In Fig. 8b, the long-term stability of the $SnO_2/Ti_3C_2T_x$ composites sensor was measured at 200 °C. The response to 100 ppm ethanol gradually decreased from 36.979 to 25.44 in the first five days, which may be due to the partial oxidation of the MXene nanosheets at 200 °C, and then stabilized at about 25 after 15 days, retaining 80% stability performances.

The sensor based on $SnO_2/Ti_3C_2T_x$ composites exhibits excellent sensing performance (36.979) to 100 ppm ethanol at 200 °C. It has good industrial application prospects compared with SnO_2 and other metal oxides based sensors that have been reported. The

Table 1
Comparison of ethanol-sensing characteristics of previously reported sensors.

Material	Temperature (°C)	Concentration (ppm)	Response value	Reference
SnO_2 hollow spheres	350	100	11	[35]
$SnO_2/Ti_3C_2T_x$ MXene	230	50	9.6	[36]
GO/SnO_2 nanofibers	300	50	28.9	[37]
SnO_2/Zn_2SnO_4	250	100	30.5	[38]
Hollow $LaFeO_3$	128	143	14.5	[39]
$Ti_3C_2T_x$ MXene	RT	100	1.7	[13]
SnO_2 /$Ti_3C_2T_x$ composites	200	100	36.979	This work

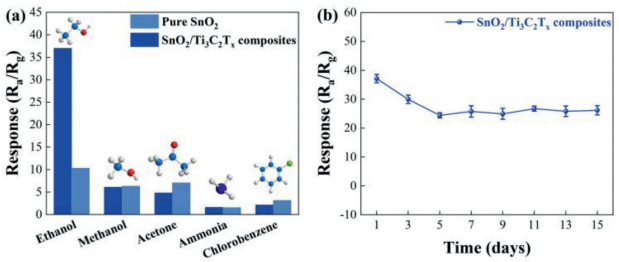

Fig. 8. (a) Gas responses of $SnO_2/Ti_3C_2T_x$ composites sensor toward 100 ppm various gases. (b) Long-term stability of the sensors based on $SnO_2/Ti_3C_2T_x$ composites to 100 ppm ethanol.

ethanol sensing characteristics of previously reported sensors are compared in Table 1.

The gas sensing mechanism of $SnO_2/Ti_3C_2T_x$ composites is usually explained by regulating the resistance of the material by adsorbing oxygen on the surface of the material. When the sensing material is exposed to air, oxygen molecules are adsorbed onto the surface of SnO_2, capturing electrons in the conduction band and turning them into oxygen ions (O_2^-, O^-, O^{2-}).

The optimal working temperature of $SnO_2/Ti_3C_2T_x$ composites is 200 °C, so most of the oxygen species adsorbed on the surface of the material exist in the form of O^- [40]. This can cause the semiconductor band to bend and form an electron depletion region. When the material is exposed to ethanol, the ethanol molecules react with the oxygen ions, especially O^-, adsorbed on the surface of the material, causing electrons to return to the conduction band. In this process, the carrier concentration increases, resulting in a decrease in the depletion layer and electrical resistance. The gas sensing response process mainly includes the following equations:

$$O_2(gas) \rightarrow O_2(ads) \quad (1)$$

$$O_2(ads) + e^- \rightarrow O_2^- \quad (2)$$

$$O_2^- + e^- \rightarrow 2O^- \quad (3)$$

$$CH_3CH_2OH(ads) + 6O^-(ads) \rightarrow 2CO_2(g) + 3H_2O(g) + 6e^- \quad (4)$$

The sensor based on $SnO_2/Ti_3C_2T_x$ composites has better sensing performances than that of pure SnO_2, which may be due to the following three reasons. Firstly, as shown in Fig. 9, the work function of $Ti_3C_2T_x$ MXene terminated with –OH (3.9 eV) is lower than that of SnO_2 (4.9 eV) reported in past work [41]. When the SnO_2 hollow nanospheres are in close contact with the $Ti_3C_2T_x$ nanosheets to equal the Fermi level, many carriers (e^-) will transfer from the $Ti_3C_2T_x$ to the SnO_2. The region where the $Ti_3C_2T_x$ loses electrons will generate positive charges, and the area where SnO_2 accepts electrons will generate negative charges, thus resulting in a depletion layer. Then, a continuous heterojunction network

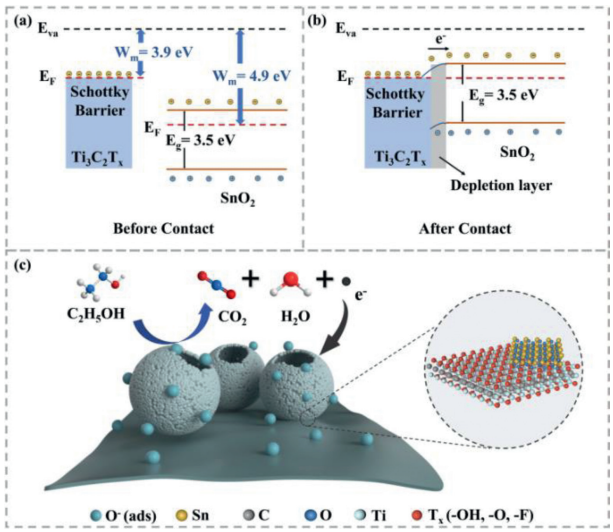

Fig. 9. Schematic illustration of gas sensing mechanism for $SnO_2/Ti_3C_2T_x$ sensors.

is formed on the surface of the material. When the composites are exposed to the target gas, the resistance changes towards a higher trend by adjusting the width of the depletion layer at the interface, and the gas sensing properties are significantly enhanced.

Secondly, the BET results show that the pore structure generates additional surface area, and the specific surface area of the $SnO_2/Ti_3C_2T_x$ composites is significantly higher than that of pure SnO_2. The increased surface area favors the creation of more active sites for gas adsorption. Besides, the hollow SnO_2 nanospheres facilitated the diffusion of gas molecules into the interior of the composite. Thus, oxygen species can be absorbed on the outer and interior shells, leading to an increase in response. Furthermore, the surface of $Ti_3C_2T_x$ is covered with a large number of functional groups (–OH, –F, and –O), which can also provide many active sites, including the adsorption site of oxygen [42]. The ethanol gas molecules adsorbed on the surface of the material will release more electrons, which is conducive to reducing the resistance and improving the sensitivity.

Thirdly, the concentration of oxygen vacancy (O_V) is also a key factor affecting gas adsorption. The XPS results show that the O_V concentration of the composites is significantly higher than that of pure SnO_2, and the increase in the O_V component means that more chemisorbed oxygen can participate in the redox reaction, increasing the favorable in-plane adsorption energy of ethanol and the level of charge transfer from the surface to ethanol [43]. Oxygen vacancies can increase the active sites on the material's surface and the electronic activity, and reduce the resistance of the sensor, thus, improving the gas interaction, response, and sensitivity. At the same time, oxygen vacancies can increase the charge density near the valence band maximum and conduction band minimum of the composite material, resulting in the reduction of the band gap, thus promoting the thermoelectric

emission and target gas adsorption/activation, and enhancing the gas sensing characteristics of the material [44,45]. So the gas sensing performance of the composites is improved.

In summary, the hollow SnO_2 nanospheres and few-layer MXene nanosheets were successfully combined by the electrostatic self-assembly, and the prepared the $SnO_2/Ti_3C_2T_x$ composites exhibit excellent sensing performances compared with pure SnO_2. The optimal working temperature of the $SnO_2/Ti_3C_2T_x$ composites is 200 °C, which is lower than that of the pure SnO_2 material (225 °C). The gas sensing response of the composites (36.979) to 100 ppm ethanol gas is higher than that of the pure SnO_2 (10.306), and the response time and recovery time are also significantly reduced. The excellent gas sensing performances of the composites are due to the unique microscopic morphology, especially the hollow nanosphere of SnO_2 providing a large number of active sites for gas adsorption. Furthermore, the increase of O_V concentration in the composites also facilitates the availability of more active sites for gas adsorption. Besides, the synergistic effect, that is combined functions which be apt to zoom up the reception and transduction of sensing signals, between SnO_2 and $Ti_3C_2T_x$ heterojunction can also promote the improvement of gas sensing performances. The combination of metal oxide semiconductor materials (MOS) and highly conductive materials such as MXene provides a feasible solution for improving ethanol gas sensing properties.

Declaration of competing interest

The authors declare that they have no known competing financial interests or personal relationships that could have appeared to influence the work reported in this paper.

Acknowledgments

This work is supported partially by the project of the State Key Laboratory of Alternate Electrical Power System with Renewable Energy Sources (Nos. LAPS21004, LAPS202114), National Natural Science Foundation of China (Nos. 52272200, 51972110, 52102245 and 52072121), Beijing Science and Technology Project (No. Z211100004621010), Beijing Natural Science Foundation (Nos. 2222076, 2222077), Hebei Natural Science Foundation (No. E2022502022), Huaneng Group Headquarters Science and Technology Project (No. HNKJ20-H88), 2022 Strategic Research Key Project of Science and Technology Commission of the Ministry of Education, China Postdoctoral Science Foundation (No. 2022M721129) and the Fundamental Research Funds for the Central Universities (Nos. 2022MS030, 2021MS028, 2020MS023, 2020MS028) and the NCEPU "Double First-Class" Program. This research was also supported by Brain Pool program funded by the Ministry of Science and ICT through the National Research Foundation of Korea (No. 2021H1D3A2A01100019). The authors would like to thank Kehui Han from Shiyanjia Lab (www.shiyanjia.com) for the XRD analysis.

Supplementary materials

Supplementary material associated with this article can be found, in the online version, at doi:10.1016/j.cclet.2023.108512.

References

[1] B.L. Rowe, P.L. Toccalino, M.J. Moran, et al., Environ. Health Perspect. 115 (2007) 1539–1546.
[2] L.F. Irvine, J. Appl. Toxicol. 23 (2003) 289–299.
[3] Y.L. Zhao, W.L. Zhang, B. Yang, et al., Nanotechnology 28 (2017) 452002.
[4] L. Zhu, W. Zeng, Sens. Actuator. A: Phys. 267 (2017) 242–261.
[5] X. Kang, N. Deng, Z. Yan, et al., Mater. Sci. Semicond. Process. 138 (2022) 106246.
[6] L. Zheng, W. Bi, Z. Jin, et al., Chin. Chem. Lett. 31 (2020) 2083–2086.
[7] R.G. Motsoeneng, I. Kortidis, R. Rikhotso, et al., Sens. Actuator. B: Chem. 316 (2020) 128041.
[8] H. Cai, X. Qiao, M. Chen, et al., Chin. Chem. Lett. 32 (2021) 1502–1506.
[9] H. Liu, X. Zhang, Y. Zhu, et al., Nanomicro Lett. 11 (2019) 65.
[10] H. Yuan, N. Li, W. Fan, et al., Adv. Sci. 9 (2022) 2104374.
[11] X. Wang, W. Liu, T. Wang, et al., Sens. Actuator. B: Chem. 350 (2022) 130876.
[12] Y. Zhao, X. Wang, T. Wang, et al., Appl. Surf. Sci. 604 (2022) 154618.
[13] S.J. Kim, H.J. Koh, C.E. Ren, et al., ACS Nano 12 (2018) 986–993.
[14] R.A. Soomro, S. Jawaid, Q. Zhu, et al., Chin. Chem. Lett. 31 (2020) 922–930.
[15] A. VahidMohammadi, J. Rosen, Y. Gogotsi, Science 372 (2021) eabf1581.
[16] W.Y. Chen, X. Jiang, S.N. Lai, et al., Nat. Commun. 11 (2020) 1302.
[17] H.C. Ji, W. Zeng, Y.Q. Li, Nanoscale 11 (2019) 22664–22684.
[18] H. Fu, Z. Feng, S.-S. Liu, et al., Chin. Chem. Lett. 34 (2023) 107425.
[19] H. Liu, L. Jiang, B. Cao, et al., ACS Nano 16 (2022) 14539–14548.
[20] Z. Yang, G. Du, Z. Guo, et al., Nanoscale 2 (2010) 1011–1017.
[21] M. Alhabeb, K. Maleski, B. Anasori, et al., Chem. Mater. 29 (2017) 7633–7644.
[22] X. Wu, Y. Gong, B. Yang, et al., Appl. Surf. Sci. 581 (2022) 152364.
[23] B. Ahmed, D.H. Anjum, Y. Gogotsi, et al., Nano Energy 34 (2017) 249–256.
[24] C. Lou, Q. Huang, Z. Li, et al., Sens. Actuator. B: Chem. 345 (2021) 130429.
[25] X. Wang, T. Wang, G. Si, et al., Sens. Actuator. B: Chem. 302 (2020) 127165.
[26] L. Wang, S. Ma, J. Li, et al., Sens. Actuator. B: Chem. 347 (2021) 130642.
[27] C. Peng, X. Yang, Y. Li, et al., ACS Appl. Mater. Interfaces 8 (2016) 6051–6060.
[28] X. Li, X. Yin, M. Han, et al., J. Mater. Chem. C 5 (2017) 4068–4074.
[29] X. Zhong, D. Wang, J. Sheng, et al., Nano Lett. 22 (2022) 1207–1216.
[30] S. Gasso, M.K. Sohal, A. Mahajan, Sens. Actuator. B: Chem. 357 (2022) 131427.
[31] X. Yuan, L. Sun, J. Wang, et al., Mater. Sci. Semicond. Process. 136 (2021) 106110.
[32] X. Dong, Q. Han, Y. Kang, et al., Chin. Chem. Lett. 33 (2022) 567–572.
[33] M. Liu, Z. Wang, P. Song, et al., Ceram. Int. 47 (2021) 23028–23037.
[34] X. Hu, X. Li, H. Yang, et al., Sens. Actuator. B: Chem. 352 (2022) 131103.
[35] B. Wang, L. Sun, Y. Wang, Mater. Lett. 218 (2018) 290–294.
[36] C. Wang, R. Li, L. Feng, et al., Chemosensors 10 (2022) 109.
[37] C.S. Reddy, G. Murali, A.S. Reddy, et al., J. Alloys Compd. 813 (2020) 152251.
[38] W. Zeng, Y. Liu, J. Mei, et al., Sens. Actuator. B: Chem. 282 (2019) 339–346.
[39] T.T. Nga Phan, T.T. My Dinh, M. Duc Nguyen, et al., Sens. Actuator. B: Chem. 354 (2022) 131195.
[40] P. Karnati, S. Akbar, P.A. Morris, Sens. Actuator. B: Chem. 295 (2019) 127–143.
[41] W. Zeng, Y. Liu, J. Mei, et al., Sens. Actuator. B: Chem. 301 (2019) 127010.
[42] M. Devaraj, S. Rajendran, T.K.A. Hoang, et al., Chemosphere 302 (2022) 134933.
[43] M. Al-Hashem, S. Akbar, P. Morris, Sens. Actuator. B: Chem. 301 (2019) 126845.
[44] H. Yuan, S.A.A.A. Aljneibi, J. Yuan, et al., Adv. Mater. 31 (2019) 1807161.
[45] X. Wang, W. Liu, C. Wang, et al., Sens. Actuator. B: Chem. 344 (2021) 130190.